

Photon Absorption Remote Sensing Virtual Histopathology: Diagnostic Equivalence to Gold-Standard H&E Staining in Skin Cancer Excisional Biopsies

Benjamin R. Ecclestone¹, James E. D. Tweel¹, Marie Abi Daoud², Hager Gaouda¹, Deepak Dinakaran³, Michael P. Wallace¹, Ally Khan Somani^{4,5}, Gilbert Bigras⁶, John R. Mackey^{6,7}, and Parsin Haji Reza¹

¹ University of Waterloo, 200 University Ave W, Waterloo, ON N2L 3G1, Canada

² University of Calgary, 2500 University Dr NW, Calgary, AB T2N 1N4, Canada

³ University of Toronto, 27 King's College Cir, Toronto, ON M5S 1A1, Canada

⁴ Indiana University School of Medicine, 550 N. University Blvd., UH 3240 Indianapolis, IN 46202

⁵ SkinMD LLC, 16105 S. LaGrange Road, Orland Park. IL 60467

⁶ University of Alberta, 116 St & 85 Ave, Edmonton, AB T6G 2R3, Canada

⁷ illumiSonics Inc, 22 King St S Suite #300, Waterloo, ON N2J 1N8, Canada

Abstract

Photon Absorption Remote Sensing (PARS) enables label-free imaging of subcellular morphology by observing biomolecule specific absorption interactions. Coupled with deep-learning, PARS produces label-free virtual Hematoxylin and Eosin (H&E) stained images in unprocessed tissues. This study evaluates the diagnostic performance of these PARS-derived virtual H&E images in benign and malignant excisional skin biopsies, including Squamous (SCC), Basal (BCC) Cell Carcinoma, and normal skin. Sixteen unstained formalin-fixed paraffin-embedded skin excisions were PARS imaged, virtually H&E stained, then chemically stained and imaged at 40x. Seven fellowship trained dermatopathologists assessed all 32 images in a masked randomized fashion.

Concordance analysis indicates 95.5% agreement between primary diagnoses rendered on PARS versus H&E images (Cohen's $k=0.93$). Inter-rater reliability was near-perfect for both image types (Fleiss' $k=0.89$ for PARS, $k=0.80$ for H&E). For subtype classification, agreement was near-perfect 91% ($k=0.73$) for SCC and was perfect for BCC. When assessing malignancy confinement (e.g., cancer margins), agreement was 92% between PARS and H&E ($k=0.718$). During assessment dermatopathologists could not reliably distinguish image origin (PARS vs. H&E), and diagnostic confidence was equivalent between the modalities.

Inter-rater reliability for PARS virtual H&E was consistent with reported benchmarks for histologic evaluation. These results indicate that PARS virtual histology may be diagnostically equivalent to traditional H&E staining in dermatopathology diagnostics, while enabling assessment directly from unlabeled, or unprocessed slides. In turn, the label-free PARS virtual H&E imaging workflow may preserve tissue for downstream analysis while producing data well-suited for AI integration potentially accelerating and enhancing the accuracy of skin cancer diagnostics.

1. Introduction

Excisional skin biopsies are a common surgical procedure performed when a suspicious skin lesion is identified (e.g., a mole with irregular features, or a non-healing ulcer), or to confirm a benign diagnosis that requires resection due to local irritation or functional impairment. During a biopsy, the lesion along with a margin of normal skin is surgically removed.^{1,2} Excised tissues are assessed through histopathological methods to confirm or rule out malignancy.¹⁻⁴ For cancerous lesions, a margin assessment is also performed to identify the adequacy of resection.³⁻⁵ A negative margin indicates the entire lesion was safely removed, while positive margins indicate that further resection is required.³⁻⁵ This process typically results in a definitive diagnosis, while achieving negative margins (complete removal) for smaller lesions, serving both diagnostic and therapeutic purposes.³⁻⁵

Photon Absorption Remote Sensing Virtual Histopathology

To enable histological analysis, skin excision samples undergo a standard tissue processing and staining procedure. Specimens are fixed in formalin, dehydrated, and embedded into paraffin wax. Embedded tissues are cut into thin translucent sections, placed onto slides, and stained with hematoxylin and eosin dyes (H&E),⁶ the gold standard stain for histological evaluation. Hematoxylin stains cell nuclei in blue-purple, while eosin colors extracellular and cytoplasmic components in shades of pink-red.⁶ This cellular microanatomy is critical for distinguishing malignant and benign skin conditions, as well as to determining the type and grade of cancer where applicable.^{3-5,7}

Despite the diagnostic value, conventional tissue processing and labelling impart certain burdens.⁶ Chemical staining carries significant costs, is time intensive, and requires technical expertise.^{6,8,9} Moreover, variability in section thickness, staining protocols, and reagent quality introduces inter-sample variability.^{6,8,9} As an alternative, there is growing interest in label-free nondestructive imaging technologies which can replicate histologic detail through fully digital “virtual staining” of unprocessed specimens. This would avoid chemical stains, enable faster turnaround, and preserve tissues for ancillary testing.

One promising technology is Photon Absorption Remote Sensing (PARS),¹⁰⁻¹³ an emerging imaging platform which observes the dominant radiative (fluorescent) and non-radiative (thermal and pressure) relaxation signatures following an optical absorption event. This method uses a pump-probe design, where the pump excites specimens using a focused picosecond-scale pulse.¹⁰⁻¹³ Then, radiative relaxation is measured as the emission of Stokes shifted photons, while non-radiative relaxation is measured as transient fluctuations in the reflected or transmitted intensity of the co-focused probe beam. By simultaneously capturing both dominant de-excitation fractions, PARS provides unique insights into biomolecules’ excited state dynamics and directly detects key biological molecules.¹⁰⁻¹³

In label-free histological imaging PARS employs (266 nm) ultraviolet (UV) excitation, to provide sensitivity to numerous diagnostic biomolecules such as hemoglobin, DNA, collagen, elastin, cytochromes.¹⁰⁻¹³ The resulting PARS absorption data can subsequently identify analogous features to traditional H&E forming a robust basis for deep learning-based virtual staining. In practice, registered and paired PARS and H&E whole-slide image datasets are used to train image-to-image translation networks, such as Pix2Pix.¹⁴ Prior work has demonstrated that PARS virtual H&E images are effectively indistinguishable from chemical staining,¹¹⁻¹³ where a recent study in breast core samples found significant pathologist agreement on diagnostic interpretation.¹²

In this prospective study, we evaluate diagnostic concordance between PARS virtual H&E staining and chemical H&E-staining, in whole slide excisional skin biopsy samples. Sixteen whole slide formalin-fixed paraffin-embedded (FFPE) skin excision samples were analyzed, representing normal skin, basal cell carcinoma (BCC), and squamous cell carcinoma (SCC). Unstained specimens were scanned using PARS to produce virtual H&E images. The same slides were then chemically H&E stained and imaged using a 40x digital pathology scanner, producing a total set of 32 whole slide images (16 PARS virtual H&E and 16 chemical H&E). Seven fellowship-trained dermatopathologists independently reviewed the whole-slide images in a masked fashion and filled in diagnostic surveys. Concordance analysis is performed to quantify the diagnostic agreement, malignancy confinement, and diagnostic confidence between the PARS virtual H&E images and the gold standard H&E-stained samples.

2. Materials and Methods

2.1. Patient Materials

A total of twenty-one independent cases of skin excisions were initially screened. A subset of sixteen formalin-fixed paraffin-embedded (FFPE) samples were selected to ensure representation across major histologic types. Five samples exhibited BCC, eight had SCC, and three were normal or benign skin tissue. Cases outside the study's scope (e.g., fungal infection) or redundant diagnoses were excluded.

The skin tissues were procured through collaboration with clinical partners. Samples were chosen from archival tissues no longer necessary for patient diagnostics, with all patient identifiers and all sample information removed. All human tissue experiments were conducted in accordance with the government of Canada TCPS2 guidelines. Specific study protocols were approved by the University of Waterloo Health Research Ethics Committee (Protocol ID: 40275; Photon Absorption Remote Sensing Microscopy of Surgical Resection, Needle Biopsy, and Pathology Specimens). As samples were fully anonymized archival tissues, the ethics committees waived informed consent.

2.2. Sample Preparation Prior to PARS Imaging and Gold Standard H&E Staining

Skin lesions were surgically excised from patients and immediately fixed in 10% neutral buffered formalin for 24 hours. After fixation, a histotechnician prepared thin sectioned histopathology slides using a standard tissue processing and embedding workflow.⁶ Specimens were dehydrated through graded ethanol rinses, cleared with xylene baths to remove ethanol and residual fats, and embedded into paraffin wax to form formalin-fixed paraffin-embedded (FFPE) tissue blocks. The FFPE blocks were sectioned with a microtome, into ~4–5 μm translucent tissue sections, which were mounted on glass microscope slides and briefly heated to 60 °C to ensure adhesion and surface uniformity.

2.3. PARS Microscope Imaging

Label-free PARS images were acquired from the unstained tissue sections using a custom-built transmission mode PARS microscope system. Detailed descriptions of the optical system, and imaging protocol are provided in a recent report by Tweel *et al.*¹³ In brief, PARS imaging was performed using a 50 kHz 400 ps 266 nm UV laser (Wedge XF 266, RPMC; Bright Solutions, Pavia, Italy) to excite biomolecules. Following each excitation, three main features were measured representing the major absorption and scattering properties: radiative (fluorescence) emission, non-radiative heating (thermal/pressure effects), and local scattering.

To quantify the radiative signal intensity, emitted Stokes shifted photons were spectrally isolated and measured with an avalanche photodiode (APD130A2; Thorlabs, Newton, NJ, USA). The radiative intensity value was recorded as the peak emission amplitude. To measure the scattering and non-radiative relaxation effects, a 405 nm continuous-wave probe beam was co-aligned with the excitation (OBIS-LS405; Coherent, Santa Clara, CA, USA). Non-radiative (photothermal, and photoacoustic) signals were measured by observing heat and pressure induced modulations in the transmitted probe beam intensity following excitation. The time-resolved non-radiative modulation was measured by integrating the modulation to determine a percentage change in probe transmission. Scattering signals were recorded by measuring the 405 nm probe transmission intensity prior to excitation (APD130A2; Thorlabs, Newton, NJ, USA).

Photon Absorption Remote Sensing Virtual Histopathology

The three optical contrasts from each excitation event then correspond to one co-registered pixel in the final image. To form images, three-axis mechanical stages moved the sample across the objective lenses in a raster (“s”-shaped) scanning pattern. Pixels or excitation events were spaced 250 nm apart achieving 40× digital imaging magnification. Matching optical resolution was provided using a 0.42 numerical aperture (NA) UV objective lens (NPAL-50-UV-YSTF; OptoSigma, Santa Ana, CA, USA) to focus both excitation and detection beams, while optical signals (probe light and radiative photons) were collected using a 0.7 NA objective lens (278-806-3; Mitutoyo, Aurora, IL, USA).

Whole slide images were formed by discretizing the ROI into 500 × 500 μm sections which were independently scanned using the highlighted method. At each section, an autofocusing operation was performed prior to scanning. Section data was then contrast matched and stitched together forming a single whole-slide image, using the pipeline outlined in by Tweel *et al.*¹³ The result was a complete whole-slide image based on native tissue absorption characteristics without the need for exogenous labels.

2.4. Gold Standard H&E Staining and Digital Image Acquisition

Following PARS imaging, all tissues samples underwent standard chemical H&E staining using standard histopathology protocols. Stained slides were digitized at 40× magnification using a transmission brightfield slide scanner (Morpholens 1; Morphle Digital Pathology, New York, NY, USA). This produced high-resolution images of the chemically stained tissue to serve as ground truth for both training and validation.

The availability of precisely aligned virtual and chemical H&E images enabled robust image-to-image model development and direct head-to-head diagnostic comparison. The use of the same slide for both modalities—PARS prior to staining, and H&E afterward—ensured matched cellular and architectural features, minimizing confounding due to sectioning artifacts or tissue heterogeneity. This method of matched image generation has been validated in previous studies.^{10–13,15}

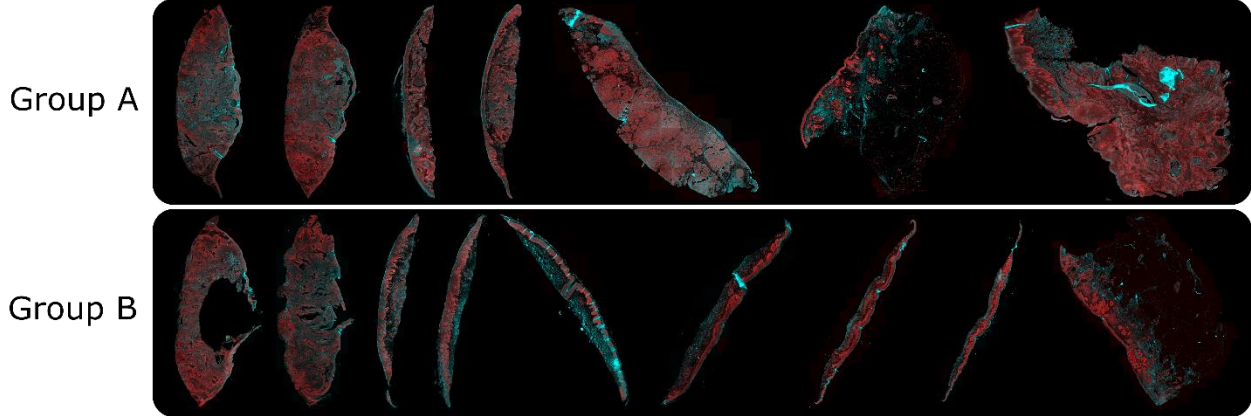
2.5. PARS Virtual H&E Colourization

A conditional generative adversarial network, Pix2Pix,¹⁴ was trained to convert PARS label-free data into virtual H&E images. This approach differs from the previous PARS virtual staining validation study, which used a cycle-consistent generative adversarial network (CycleGAN).^{12,16} CycleGAN does not require registration between the ground truth, and target domain.^{12,17} As a result, CycleGAN may provide more optimal virtual staining performance (e.g., superior image clarity and sharpness) in samples where it is difficult to provide pixel-level ground truth (such as the previously explored need-core biopsy samples).^{12,14,16,17} However, if pixel-level registration is possible, Pix2Pix can provide more robust correlations between structure and color, facilitating an improved domain transformation and better virtual staining image quality.^{14,16} The key challenge to date has been developing a sufficient volume of pixel-level registered whole slide image data for model training. To this end, this work utilizes a new WSI registration workflow, based on the Warpy framework.²³ This enables pixel-level whole slide registration, facilitating successful implementation of the Pix2Pix virtual staining models.

In this study, two Pix2Pix virtual staining models were trained and applied to colorize the 16 whole slide virtual H&E images. Model 1 excluded Group A slides during training and was applied only to Group A; Model 2 excluded Group B and was applied to Group B (Figure 1a). This ensured that colorization was performed only on unseen data, supporting robust validation.

Photon Absorption Remote Sensing Virtual Histopathology

(a) Tissue Selections for Model Training



(b) Virtual Staining: Training and Colorization Workflow

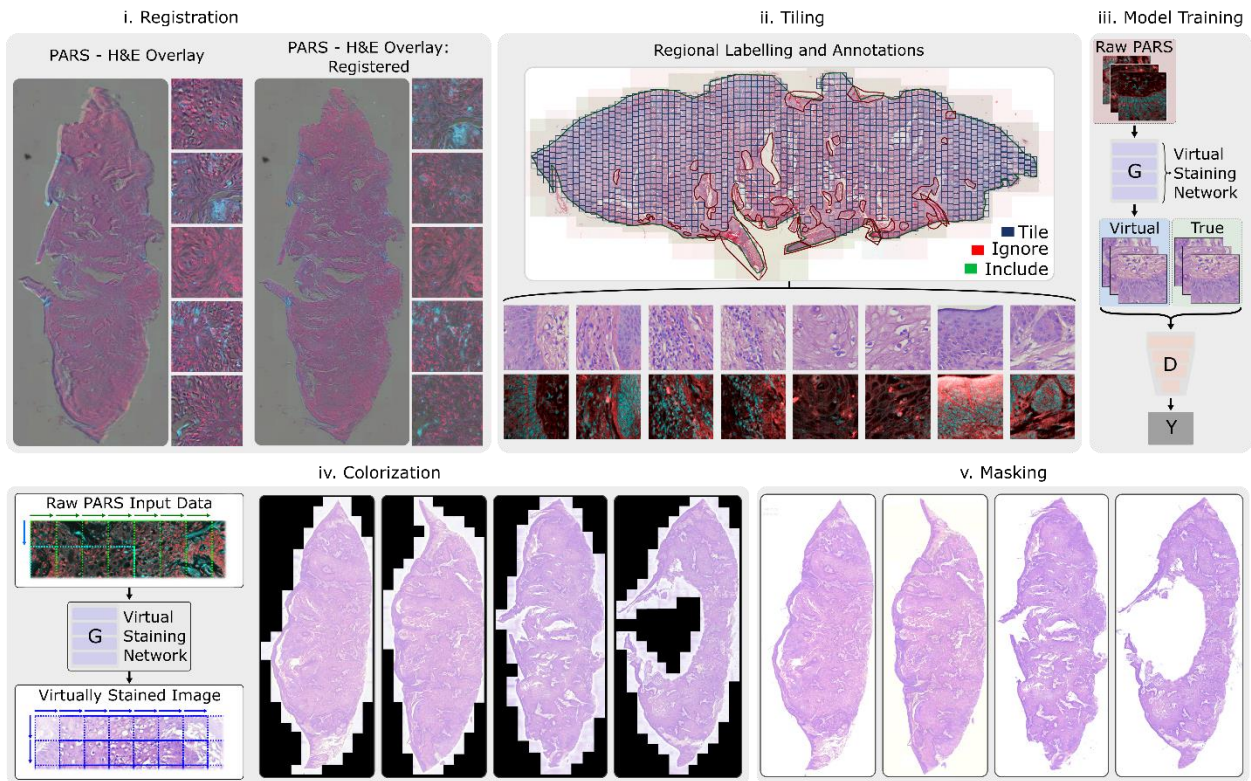


Figure 1. Workflow for developing PARS virtual H&E images. (a) Division of data for network training and colorization. Model (1) excluded data from Group A for training, while Model (2) excluded data from Group B during training. Models were then applied to virtually stain the respective groups ensuring only unseen data was colorized. (b) Steps performed to train and colorize tissues including, (i) whole slide registration using the Warpy whole slide registration workflow,¹⁸ (ii) data labelling and (512 x 512 pixel) training pair generation, (iii) algorithm training, (iv) colorization or model application using 75% linearly blended overlapping regions, and (v) masking to conceal unscanned areas.

Preparing the two Pix2Pix virtual staining models and developing the virtually stained images involved the following key steps (Figure 1(b)) (i) registration, (ii) tiling, (iii) training, (iv) colorization, (v) masking. Whole slide images (H&E and PARS) were registered using the Warpy workflow, which features manual rigid registration, automated affine registration, and a patchwise (500 × 500 μm patches) spline registration.¹⁸ An example of slide overlays before and after registration are shown in Figure 1(b-i). Registered whole slide images were annotated to identify the tissue, and exclude artifacts (e.g., out of

Photon Absorption Remote Sensing Virtual Histopathology

focus regions). Annotations were used to dice images into 512 × 512-pixel (128 × 128 μm) tile pairs (Figure 1(b-ii)) for model training. Model (1) used a total of 11459 training pairs, while Model (2) used a total of 11232 training pairs. Training was performed over 200 epochs, on a Nvidia RTX A6000 using pytorch 2.3.1 and Cuda 11.8 (Figure 1(b-iii)). Model (1) was applied to virtually stain the 7 unseen slides of Group (A), while Model (2) was applied to the 9 unseen slides from Group (B), resulting in 16 colorized whole slide images (Figure 1(b-iv)). During the colorization the model was applied to overlapping 512 × 512-pixel patches, which were linearly blended. Both PARS virtual H&E, and the ground truth H&E images were then masked (Figure 1(b-v)) to hide unscanned regions and remove background features (e.g., dust) which could indicate the image origin.

2.6. Evaluation by Expert Pathologists

Seven fellowship trained dermatopathologists, six with no prior exposure to PARS virtual histology images, independently reviewed the 32 images (16 PARS and 16 H&E) using a customized web-based histopathology platform. Reviewers could freely navigate and zoom (up to 40×) each slide using the web interface. Pathologist scored each image on the parameters shown in Table 1.

Images were anonymized, randomly rotated, and assigned alphanumeric reference labels of AA through BF for survey purposes. All clinicopathologic details of the cases and the origin of the digital images (either true chemical H&E or PARS virtual H&E) were masked. Slides were presented in the following algorithmically randomized order: T16, T13, P8, T2, P4, P9, T14, P3, T6, T15, T12, P5, T11, P7, T1, T3, T10, P14, T8, T4, P11, T9, P6, P12, T7, P10, P15, P16, P13, P1, T5, P2. The ‘P’ prefix corresponds to PARS virtual H&E, while the ‘T’ prefix corresponds to true chemical H&E. This presentation sequence was designed using an algorithm which randomized image order while ensuring independent PARS and true H&E images from the same tissue were presented at least 7 images apart. The aim was to minimize potential for biases within each image pair, which might arise if (for example) an image pair from the same tissue were shown back-to-back.

Table 1. Survey questionnaire given to pathologists for each of the 32 images.

1. The primary tissue diagnosis is:	<input type="checkbox"/> Non-Malignant/ Benign <input type="checkbox"/> Squamous Cell Carcinoma <input type="checkbox"/> Basal Cell Carcinoma <input type="checkbox"/> Melanoma
2. Squamous Cell Carcinoma	<input type="checkbox"/> in situ SCC only <input type="checkbox"/> well differentiated SCC <input type="checkbox"/> moderately differentiated SCC <input type="checkbox"/> poorly differentiated SCC
3. Basal Cell Carcinoma	<input type="checkbox"/> Low Risk * <input type="checkbox"/> High Risk †
4. Melanoma	<input type="checkbox"/> High Dermal Mitotic Rate <input type="checkbox"/> Skin Ulceration <input type="checkbox"/> Desmoplastic melanoma <input type="checkbox"/> Lymphatic invasion <input type="checkbox"/> Brisk Tumor Infiltrating Lymphocytes

Photon Absorption Remote Sensing Virtual Histopathology

5. Malignancy confined within the boundaries of the tissue in this section / margins negative	<input type="checkbox"/> Yes
	<input type="checkbox"/> No
6. This digital image comes from H&E	<input type="checkbox"/> Yes
	<input type="checkbox"/> No
	<input type="checkbox"/> Uncertain
7. My diagnostic confidence is	<input type="checkbox"/> Low
	<input type="checkbox"/> Moderate
	<input type="checkbox"/> High

* e.g., nodular, superficial, pigmented, infundibulocystic, fibroepithelial
† e.g., basosquamous, sclerosing/morpheaform, keloidal, infiltrative, sarcomatoid

2.7. Statistical Analysis

Agreement between PARS and H&E diagnoses was quantified using Cohen's kappa (κ) (for intra-rater modality comparison) and Fleiss' kappa (κ) (for inter-rater agreement within each modality). The Cohen's kappa coefficient measures inter-rater reliability while accounting for the possibility of agreement occurring by chance.¹⁹ This is key to assessing if two raters agree beyond what would be expected by chance alone. The Kappa assessment also provides robustness to varied prevalences in different data categories.¹⁹ The Fleiss' kappa measures the same characteristic as the Cohen's kappa but compares more than two raters.²⁰

Kappa values range from -1 to 1 . Positive values indicate agreement beyond chance (1 indicates perfect agreement), while negative values indicate agreement worse than chance. Kappa values were interpreted as "fair" or "poor" for $\kappa < 0.6$, "substantial" or "good" for $\kappa = 0.6 - 0.8$, "near perfect" for $\kappa > 0.8$.^{21,22} Percent agreement metrics were also reported to contextualize kappa scores. All calculations were performed in R statistical software (version 4.2.0).²³

3. Results

3.1. Example Whole-Slide Image Pairs

Representative whole-slide images from two skin excision specimens are shown in Figures 2 and 3. For each tissue sample, the raw total absorption (TA) PARS image is presented alongside the PARS virtual H&E, and real H&E image. In the TA PARS image, the radiative relaxation is colored in blue, while the non-radiative relaxation is colored red. This image represents the raw PARS data which is inputted into the virtual staining algorithm. The virtual and chemical H&E images represent the diagnostic views shown to pathologists during assessment.

Figure 2 illustrates a case of basal cell carcinoma (BCC). High-magnification views (Fig. 2i–ii) reveal classic basaloid nests and cords with hyperchromatic nuclei, scant cytoplasm, and peripheral nuclear palisading. These tumor clusters are embedded in a mucinous or fibroblastic stroma, consistent with nodular or superficial BCC. The absence of keratinization distinguishes BCC from squamous cell carcinoma, where mitotic figures are common but rarely atypical.

Figure 3 depicts squamous cell carcinoma (SCC). Higher magnification (Fig. 3i–ii) shows atypical keratinocytes with pleomorphic, hyperchromatic nuclei and prominent keratinization. Features include dyskeratotic cells, keratin pearls, and intercellular bridges—all hallmarks of squamous differentiation. SCC

Photon Absorption Remote Sensing Virtual Histopathology

invades the dermis in sheets, cords, or nests, with variable differentiation. Well-differentiated tumors show organized keratinization, while poorly differentiated lesions lack keratin and exhibit marked nuclear atypia and mitotic activity. Desmoplastic stroma may surround invasive nests, especially in aggressive variants.

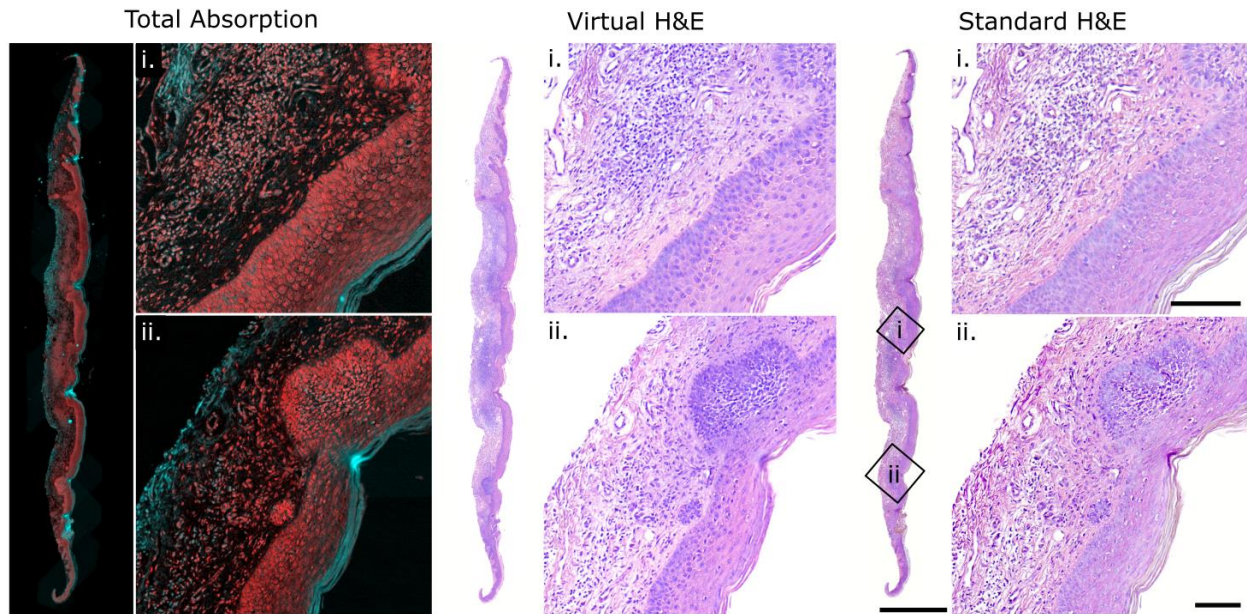


Figure 2. Example PARS total absorption (TA), virtual H&E, and true H&E pair used in this study. The sample exhibits closely matched staining colours and tissue morphology between the virtual and real representations. Scale Bar: 1 mm. Sub figures (i,ii) depict two regions of higher magnification on the sample. Scale Bar: 100 μm .

Comparing the different visualizations, the “Total-Absorption” (TA) PARS images provide a clear basis for the success of the virtual staining. The deep UV excitation used in PARS is broadly absorbed in tissues, where the unique distribution of relaxation effects (radiative vs. non-radiative) provides specificity to critical diagnostic features. The non-radiative contrast (red) highlights predominately DNA which exhibits strong non-radiative relaxation, corresponding to similar features as hematoxylin staining. Conversely, the connective tissues (primarily collagen and elastin) exhibit appreciable radiative relaxation (blue) approximating eosin’s affinity for cytoplasm and stroma.^{10–13} In some instances, PARS may reveal additional features which are not visualized by the H&E staining. For example, the inner elastic wall of an artery exhibits prominent radiative signal (Figure 3 TA-i) not captured in standard H&E due to limited sensitivity to certain biomolecules. The virtual staining model suppresses these features to match the chemical H&E fidelity.

An additional advantage of the PARS virtual staining is contrast consistency. In PARS the signal (and virtual H&E stain contrast) is derived from the endogenous absorption. Hence, the virtual staining exhibits uniformity across all samples. In contrast, chemical H&E staining is subject to variability from factors such as section thickness, dye concentration, staining duration, specimen age, and storage conditions.^{24–28} This improved consistency with virtual staining may support improved reproducibility in digital workflows.

As a further extension, while this work focuses only on virtual H&E staining, there are numerous other stains used in clinical settings. As an example, virtual staining networks could be trained to develop Periodic Acid Schiff and Toluidine Blue which are used to in certain cases of basaloid carcinomas.^{42,43} In

Photon Absorption Remote Sensing Virtual Histopathology

this work, H&E was selected to align with current practices for skin malignancy diagnosis. The turnaround for a pathology report is typically a week or more due to tissue preparation, chemical H&E staining, brightfield imaging, and human diagnostic interpretation. Hence, the additional stains beyond H&E are often avoided to mitigate further delays. However, each PARS scan of a single unstained slide generates rich, multidimensional molecular data that has the potential to replicate several chemical staining patterns. With the development of additional virtual staining models. Multiple stains may be developed from each tissue specimen. In addition, the label-free imaging retains samples ancillary testing and analysis.

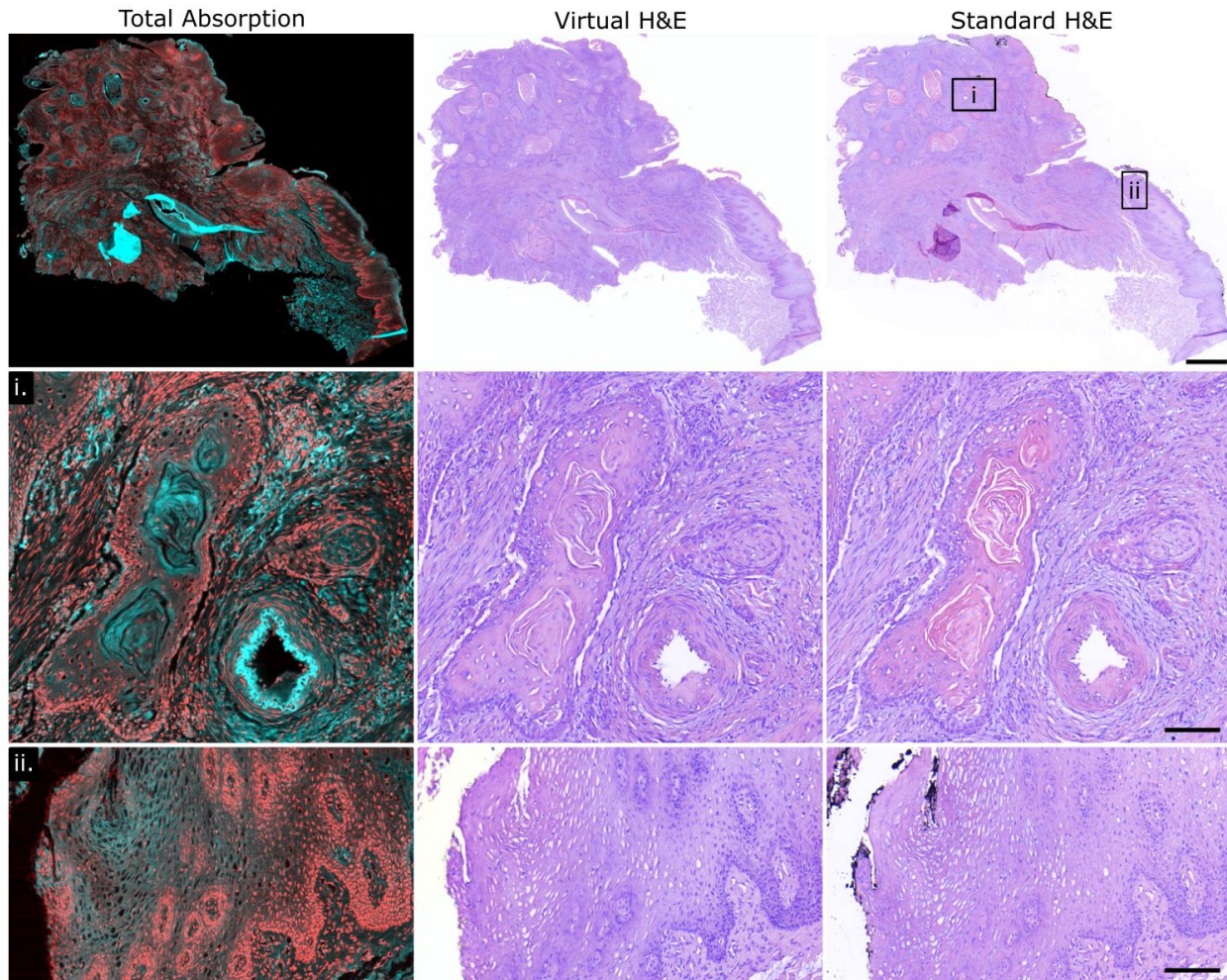


Figure 3. Example PARS total absorption (TA), virtual H&E, and true H&E pair used in this study. Both the virtual and real H&E images exhibit excellent epithelial and stromal contrast and highlight the same tissue structures. Scale Bar: 1 mm. Sub figures (i,ii) depict two regions of higher magnification on the sample. Scale Bar: 100 μ m.

3.2. Primary Diagnosis

Pathologists were first asked to assign a primary diagnosis for each image (PARS, and H&E), resulting in 32 (16 PARS and 16 H&E) preliminary diagnoses per rater, for a total of 224 primary diagnoses (Table 2). Inter-rater agreement was high within each modality (Fleiss' kappa $\kappa = 0.886$ for PARS and Fleiss' kappa $\kappa = 0.805$ for H&E). This indicates near perfect inter-rater agreement for diagnosis within the PARS and within the H&E images.

Photon Absorption Remote Sensing Virtual Histopathology

Inter-modality agreement between the PARS and H&E was similarly strong. Across raters the average diagnostic concordance between PARS and H&E was 95.5% , with a Cohen’s kappa ($\kappa = 0.93$) indicating near-perfect agreement. In total, basal’ was chosen 63 times, ‘non-malignant’ 45 times, ‘squamous’ 113 times, and ‘melanoma’ 3 times. There were a total of 5 disagreements on diagnoses between an H&E and PARS pair. Three pathologists had perfect agreement ($\kappa = 1$), while the remaining four had near-perfect agreement ($\kappa = 0.8-0.9$). These results indicate reliable and equivalent diagnostic discrimination between BCC, SCC, melanoma, and benign lesions across modalities.

Table 2. Summary of pathologist responses to question “The primary tissue diagnosis is”.

		H&E Diagnosis				Total
		SCC	BCC	Melanoma	Benign	
PARS Diagnosis	SCC	56	-	-	-	56
	BCC	-	30	-	2	32
	Melanoma	-	-	1	-	1
	Benign	1	1	1	20	23
	Total	57	31	2	22	112

3.3. Evaluation of Cancer Subtypes and Grading

A similar analysis to the primary diagnosis response was performed to assess the concordance for the evaluation of the malignant subtypes, as per the Table 1 criterion for each of the cancers.

3.3.1 Squamous Cell Carcinoma:

SCC was diagnosed 113 times (the number is uneven due to a discordant diagnosis between the PARS and H&E as noted in the *Primary Diagnosis* section). The SCC subtyping responses were as follows ‘well differentiated’ (n = 68) or ‘moderately differentiated’ (n = 39), with ‘poorly differentiated’ (n = 3) and ‘in situ’ (n = 3) rarely chosen (Table 3).

Inter-rater agreement was measured using the 7 cases where there was complete agreement of the SCC primary diagnosis. The Fleiss’ kappa for inter-rater agreement was computed as $\kappa = -0.0121$ for the H&E images, and $\kappa = 0.0392$ for the PARS images. This indicates no inter-rater agreement between pathologists within the H&E images, or within the PARS images.

Despite low inter-rater agreement, intra-rater agreement between matched H&E–PARS pairs showed 91% concordance with a mean Cohen’s κ of 0.73. This suggests individual raters preserved consistent subtype interpretations across the PARS and H&E image pairs. As an aside, rater 1 exhibited a very low kappa ($\kappa = 0$) despite exhibiting a 5/7 success rate. This is an effect of calculating the Kappa statistic with a relatively low sample size.

Table 3. Summary of pathologist responses to the question of the Squamous Cell Carcinoma Subtyping.

Rater	Agreements	Total SCC Selections	Kappa
1	5	7	0.0
2	6	8	0.5
3	9	9	1
4	8	8	1

Photon Absorption Remote Sensing Virtual Histopathology

5	8	8	1
6	7	8	0.619
7	8	8	1
Total	51	56	0.73

3.3.2 Basal Cell Carcinoma:

BCC was selected as the primary diagnosis 63 times. Excluding 3 instances of discordant diagnosis between H&E and PARS image pairs (i.e., ‘basal’ was selected for one image and not the other (Table 2)), 60 matched image sets remained. Of these responses 58 gradings were ‘low’ and just 2 were ‘high’. The two ‘high’ responses are attributed to Rater 4, on a matching set of PARS and H&E images. Therefore, the PARS and H&E yielded 100% agreement between matched virtual and chemical H&E for BCC grading.

3.3.3 Melanoma:

Melanoma was selected only three times (Rater 1: 2; Rater 6: 1), with subtype features reported once. Due to low frequency, no conclusions were drawn.

3.4. Evaluation of Cancer Margins/Tissue Edges

If pathologists identified malignancy (BCC, SCC, Melanoma), they were asked to assess the resection margins. Malignancy confined within the boundaries of the tissue corresponds to negative margins indicating a complete resection. Of 179 malignant diagnosis, 178 responses were recorded: 140 “no” and 38 “yes”.

Inter-rater agreement was high within the H&E, and within the PARS images, corresponding to a Fleiss’ kappa of $\kappa = 0.784$ for H&E images, and $\kappa = 0.824$ for PARS images. This was calculated using the 10 image pairs which exhibited universal malignancy diagnosis (i.e., all 7 raters selected BCC, SCC, or Melanoma). Other tissues were benign ($n = 3$) or had less than 100% agreement in the primary diagnosis ($n = 3$). Within this set of 10 tissues, all disagreements of margin assessment occurred on a single H&E and PARS pair. Responses were (4 ‘yes’: 3 ‘no’) for the H&E, and (6 ‘yes’: 1 ‘no’) for the PARS. This suggests that this sample was difficult to assess, potentially due to poor tissue selection or poor specimen quality. Excluding this case, there was perfect inter-rater agreement during margin assessment within the PARS and within the H&E images.

Table 4. Summary of pathologist responses to the question of malignancy confinement.

Rater	Agreements	Total Margin Selections	Kappa
1	10	10	1
2	11	13	0.409
3	12	14	0.44
4	13	13	1
5	12	12	1
6	10	12	0.429
7	11	12	0.75
Total	79	86	0.718

Photon Absorption Remote Sensing Virtual Histopathology

Inter-modality concordance was similarly high between the PARS and H&E during margin assessment. The average inter-modality agreement was 92%, with Cohen's $\kappa = 0.718$. This is calculated using the sample pairs where each pathologist had a concordant diagnosis. This indicates significant agreement of margin assessment between the PARS and H&E images.

3.5. Image Origin

Raters were asked to classify image origin as a chemical H&E, virtual (PARS) or uncertain (Table 5). The option “uncertain” was chosen most often (86/224), indicating pathologists were frequently unsure of the image origin. The fourth respondent selected ‘Uncertain’ for all 16 PARS and 16 H&E images. Among the other raters, there were 25 instances H&E images were misidentified as virtual (PARS), and 38 instances where virtual H&E was misidentified as real images.

Raters were only slightly more likely to consider H&E images genuine (40%) than virtual (34%). These suggest that pathologists could not reliably distinguish between conventional H&E and PARS virtual H&E.

Table 5. Summary of pathologist responses to question “This digital image comes from H&E”.

Image	Response	Rater							Total
		1	2	3	4	5	6	7	
H&E	Genuine	10	0	9	0	11	12	3	45
	Uncertain	1	11	0	16	2	0	12	42
	Virtual	5	5	7	0	3	4	1	25
PARS	Genuine	10	0	6	0	7	13	2	38
	Uncertain	3	9	2	16	2	0	12	44
	Virtual	3	7	8	0	7	3	2	30

3.6. Diagnostic Confidence

Respondents were asked to rate their diagnostic confidence as Low, Moderate, or High (Table 6). Of 224 total responses, 167 were high, 42 moderate, and 15 low. Inter-rater agreement was found to be fair within the PARS (Fleiss’ kappa $\kappa = 0.235$), and within the H&E images (Fleiss’ kappa $\kappa = 0.264$).

Inter-modality agreement was also calculated to compare raters diagnostic confidence between image pairs. The average Cohen's kappa across raters was $\kappa = 0.36$ indicating fair agreement of diagnostic confidence between the PARS and H&E images. There were 23 cases where a raters diagnostic confidence differed within a PARS and H&E image pair. Of the disagreements, 11/23 favored the PARS image, while 12/23 favored the H&E images.

Table 6. Summary of pathologist responses to the question “My diagnostic confidence is”

Score	H&E	PARS	Total
Low	8	7	15
Moderate	20	22	42
High	84	83	167
Kappa	0.264	0.235	

4. Discussion

4.1. Study Summary and Key Findings

This study evaluated the diagnostic performance of PARS-generated virtual H&E images compared to conventional chemical H&E staining in excised skin tissue specimens. Sixteen unstained FFPE skin excisional biopsies were imaged using PARS, virtually stained, then chemically labelled with H&E and digitally scanned at 40× magnification. The resulting 32 images were assessed by seven fellowship-trained dermatopathologists in a masked and randomized fashion. Pathologists evaluated freely evaluated diagnostic features across the entire whole slide images (with the image origin masked), at any magnification (up to 40x).

Across all diagnostic metrics (i.e., primary diagnosis, tumor subtype, and malignancy confinement) PARS images demonstrated significant concordance (>90% agreement, with a $\kappa > 0.7$) comparable to, or exceeding, chemical H&E evaluation of the same tissue section.

For the primary diagnosis, raters showed near perfect inter-rater agreement within PARS ($\kappa = 0.886$) and within H&E images ($\kappa = 0.805$). Inter-modality agreement was even stronger between the PARS and H&E images with a total 95.5% agreement (Kappa 0.93). Substantial concordance was also achieved when malignancy subtype or grade. For SCC subtyping, there was 91% inter-modality agreement ($\kappa = 0.73$) between the PARS and H&E images. For BCC subtyping, there was perfect agreement amongst all raters. Melanoma, which was not imaged in this case series but was given as a distractor option on the questionnaire, was only selected 3 times, and the low frequency did not permit statistical analysis. When assessing resection margins, there was substantial inter-rater agreement within the H&E ($\kappa = 0.784$), and PARS ($\kappa = 0.824$). There was also substantial inter-modality agreement (92% with $\kappa = 0.718$) between PARS and H&E.

Importantly, raters were unable to reliably distinguish virtual from real H&E images, and the diagnostic confidence was similar for each modality. In some measures, such as margin assessment (PARS: $\kappa = 0.824$, H&E $\kappa = 0.784$), or primary diagnosis (PARS: $\kappa = 0.886$, H&E $\kappa = 0.805$), PARS even slightly outperformed the chemical H&E images. This suggests that PARS virtual staining may enable more consistency in diagnosis as compared to the H&E images. These differences may reflect an improvement in stain standardization, as virtual staining eliminates the variability associated with chemical protocols such as section thickness, reagent quality, and staining duration.^{6,8,9} Overall, this analysis strongly supports the conclusion that PARS virtual H&E images provide diagnostic performance that matches or exceeds conventional H&E images.

4.2. Interpretation of Findings in Context

While chemical H&E staining remains the diagnostic gold standard, it is subject to interobserver variability and process-related inconsistencies. Developing a diagnosis often requires assessment of subtle features of nuclear morphology and tissue organization.³⁰⁻³³ This complicates the evaluation of new histologic techniques, such as PARS virtual H&E images, since the “gold standard” chemical H&E assessment is itself imperfect. In the context of this study, PARS virtual histology in skin excisions is shown to be diagnostically equivalent to chemical H&E staining assessed through digital histopathology.

Photon Absorption Remote Sensing Virtual Histopathology

Diagnostic concordance for common skin cancers such as BCC and SCC is generally high.^{34,35} Well-defined and common diagnoses often report agreement exceeding 90% in many cases.^{34,35} This aligns with our findings for the primary diagnosis, which exhibited high inter-rater agreement (PARS: $\kappa = 0.886$, H&E $\kappa=0.805$) and high diagnostic concordance (95.5% agreement, $\kappa = 0.93$). Though, performance can vary depending on the complexity or rarity of the lesion, and the pathologist specialization.³⁶

In this study, there was significant inter-modality between the PARS and H&E (91%, $\kappa = 0.73$) for the SCC subtype, despite poor inter-rater agreement (H&E $\kappa = -0.0121$, PARS $\kappa = 0.0392$). Concurrently, the diagnostic confidence exhibited only fair inter-rater agreement (PARS: $\kappa = 0.235$, H&E: $\kappa = 0.264$), with a nearly identical distribution of confidence scores across PARS and H&E. This indicates that despite the potential variability between individual pathologists' interpretation PARS offers comparable interpretability and diagnostic confidence to chemical H&E images.

Despite high overall concordance for common skin cancers, variability remains a concern for rare subtypes or lesions at the interface of benign and malignant features. This illustrates the importance of new methods and improvements to diagnostic tools which may enhance reliability and accuracy. As an example, virtual staining could help to reduce pre-analytic variations. Unlike chemical staining, which is sensitive to section thickness, tissue processing, and reagent variability, PARS produces consistent stain outputs.^{6,8,9} This standardization may explain the high inter-rater agreement observed for PARS across multiple diagnostic tasks. Coupled with emerging technologies in AI diagnostics, PARS has significant potential to enhance these diagnostic processes.³⁸⁻⁴⁰

3. Strengths, Limitations, and Future Research

Careful consideration was taken to minimize factors which could unduly influence pathologist responses. Pathologists were carefully masked to tissue origin. Images were randomly oriented and randomly ordered with an enforced minimum spacing between image pairs. Image backgrounds were removed to further mask the underlying modality. In addition, every effort was made to ensure that standard diagnostic practices were facilitated. Pathologists were allowed to freely assess the 40× digital histology images as they would during conventional workflows. Efforts were also taken to minimize confounding effects from sample variance. PARS and H&E images were derived from exactly same tissue sections, rather than adjacent slides, ensuring direct nuclei to nuclei pairing and identical diagnostic features in each image.

The conclusions presented here are encouraging but limited by sample size of tissues ($n = 16$ slides), and pathologists ($n = 7$ raters). The diagnostic scope also limits the generalization by focusing on the most common skin lesions (BCC and SCC).

Future studies should expand the number of raters and increase the number of samples to further generalize and expand upon the findings presented here. Other studies should also expand the diagnostic scope to incorporate melanocytic lesions and additional cancer subtypes, as well as to include other major cancer types, such as gastrointestinal cancers. In addition, future studies should include additional histochemical stains. Given the unique absorption data captured by PARS, there is potential for PARS to provide multiplexed virtual staining contrasts, where several virtual stains may be produced from a single PARS scan of tissues.^{42,43} Finally, future studies should focus on additional sample formats. While, the present study focuses on FFPE specimens, PARS has previously shown capability to image thick unstained specimens including bulk unprocessed tissues.¹⁰ Future works may explore using PARS to provide virtual staining (e.g., H&E) directly within bulk unprocessed tissues (freshly resected, or preserved).

5. Conclusions

PARS label-free virtual histology imaging offers a promising alternative to chemical staining workflows. By observing the dominant radiative (fluorescent) and non-radiative (thermal) relaxation processes following an optical absorption event, PARS generates rich datasets which are a strong starting point for artificial intelligence imaging and diagnostic methods. It enables label-free virtually stained images which are diagnostically equivalent to H&E across major metrics. Pathologists interpreted PARS images with similar confidence and accuracy and could not reliably distinguish image origin.

The results of this current study add to a growing body of work which indicate that PARS virtual H&E imaging may be applicable to histological evaluation with the ultimate goal of generalized H&E diagnostic capacity.¹¹⁻¹³ PARS imaging has potential to transform histologic workflows by reducing time, and cost. In addition, PARS may enhance diagnostics by reducing tissue consumption to allow ancillary diagnostic testing, while producing datasets which enable seamless integration towards AI diagnostics.

Future extensions of this work include larger multi-institutional validation studies, exploration of broader staining repertoires, and exploration of additional malignancies and tissue types. Ultimately, as PARS directly targets endogenous contrast of the tissues, this technique can be applied to any form of tissue, including freshly resected specimens,¹⁰ and living tissues *in vivo*.⁴⁴ As a result, the PARS virtual histology could be applied to image freshly resected tissues (e.g., Mohs surgical resections).

In aggregate, the high-fidelity virtual histology capabilities PARS imaging stands to transform the landscape of digital pathology.

Institutional Review Board Statement: Tissues were acquired through collaboration with clinical partners. Specimens were acquired under protocols (Protocol ID: HREBA.CC-18-0277) with the Research Ethics Board of Alberta and (Photoacoustic Remote Sensing Microscopy of Surgical Resection, Needle Biopsy, and Pathology Specimens; Protocol ID: 40275) with the University of Waterloo Health Research Ethics Committee. All human tissue experiments were conducted in accordance with the government of Canada guidelines and regulations, including “Ethical Conduct for Research Involving Humans (TCPS2)”.

Informed Consent Statement: The samples were obtained from anonymous patient donors, with all patient identifiers removed to ensure anonymity. The ethics committee waived the need for patient consent as these archival tissues were no longer necessary for patient diagnostics. Researchers were not provided with any information pertaining to the identity of the patients.

Data Availability Statement: Datasets used and analyzed during this study are available from the corresponding author on reasonable request.

Acknowledgments: The authors thank Drs. David Beyer, Karen Naert, Ami Wang, Pavandeep Gill, Xiao Zhu, and Calvin Tseng for participating in the survey and questionnaire.

Conflicts of Interest: The authors JEDT, BRE, HG, DD, JRM, and PHR all have financial interests in IllumiSonics, which has provided funding to the PhotoMedicine Labs. The authors MAD, AKS, MPW and GB do not have any competing interests. The assessment data were generated by pathologists masked to

Photon Absorption Remote Sensing Virtual Histopathology

the image origin, and these pathologists have no financial interest in the outcomes of the study. The image order was randomized with guidance from MPW, the statistician analyzed the study; MPW also has no financial interests in the outcomes. All the data gathered were included in the analysis. The raw dataset, generated using SurveyMonkey, was directly provided to the statistician.

References:

1. Beard C j., Ponnarasu S, Campos MBS, Schmieder GJ. Excisional Biopsy. *JAMA: The Journal of the American Medical Association*. 2025;244(1):30. doi:10.1001/jama.1980.03310010020019
2. Kansara S, Bell D, Weber R. Surgical management of non melanoma skin cancer of the head and neck. *Oral Oncol*. 2020;100:104485. doi:10.1016/J.ORALONCOLOGY.2019.104485
3. Alam M, Armstrong A, Baum C, et al. Guidelines of care for the management of cutaneous squamous cell carcinoma. *J Am Acad Dermatol*. 2018;78(3):560-578. doi:10.1016/J.JAAD.2017.10.007
4. Bichakjian C, Armstrong A, Baum C, et al. Guidelines of care for the management of basal cell carcinoma. *J Am Acad Dermatol*. 2018;78(3):540-559. doi:10.1016/J.JAAD.2017.10.006
5. Nahhas AF, Scarbrough CA, Trotter S. A Review of the Global Guidelines on Surgical Margins for Nonmelanoma Skin Cancers. *J Clin Aesthet Dermatol*. 2017;10(4):37.
6. Feldman AT, Wolfe D. Tissue processing and hematoxylin and eosin staining. *Methods in Molecular Biology*. 2014;1180:31-43. doi:10.1007/978-1-4939-1050-2_3/COVER
7. Cives M, Mannavola F, Lospalluti L, et al. Non-Melanoma Skin Cancers: Biological and Clinical Features. *Int J Mol Sci*. 2020;21(15):5394. doi:10.3390/IJMS21155394
8. Brown L. Improving histopathology turnaround time: a process management approach. *Curr Diagn Pathol*. 2004;10(6):444-452. doi:10.1016/J.CDIP.2004.07.008
9. Munari E, Scarpa A, Cima L, et al. Cutting-edge technology and automation in the pathology laboratory. *Virchows Archiv*. 2024;484(4):555-566. doi:10.1007/S00428-023-03637-Z/TABLES/3
10. Ecclestone B, Bell K, Sparkes S, Dinakaran D, Mackey J, Haji Reza P. Label-Free Complete Absorption Microscopy Using Second Generation Photoacoustic Remote Sensing. Published online October 9, 2021. doi:10.21203/RS.3.RS-887767/V1
11. Bektor M, Ecclestone BR, Pekar V, et al. Virtual histological staining of label-free total absorption photoacoustic remote sensing (TA-PARS). *Scientific Reports 2022 12:1*. 2022;12(1):1-12. doi:10.1038/s41598-022-14042-y
12. Tweel JED, Ecclestone BR, Gaouda H, et al. Photon Absorption Remote Sensing Imaging of Breast Needle Core Biopsies Is Diagnostically Equivalent to Gold Standard H&E Histologic Assessment. *Current Oncology 2023, Vol 30, Pages 9760-9771*. 2023;30(11):9760-9771. doi:10.3390/CURRONCOL30110708

Photon Absorption Remote Sensing Virtual Histopathology

13. Tweel JED, Ecclestone BR, Boktor M, Dinakaran D, Mackey JR, Reza PH. Automated Whole Slide Imaging for Label-Free Histology Using Photon Absorption Remote Sensing Microscopy. *IEEE Trans Biomed Eng.* 2024;71(6):1901-1912. doi:10.1109/TBME.2024.3355296
14. Tahmid M, Alam MS, Rao N, Ashrafi KMA. Image-to-Image Translation with Conditional Adversarial Networks. *Proceedings of 2023 IEEE 9th International Women in Engineering (WIE) Conference on Electrical and Computer Engineering, WIECON-ECE 2023.* Published online November 21, 2016:468-472. doi:10.1109/WIECON-ECE60392.2023.10456447
15. Ecclestone BR, Dinakaran D, Mackey JR, et al. Histopathology for Mohs micrographic surgery with photoacoustic remote sensing microscopy. *Biomedical Optics Express, Vol 12, Issue 1, pp 654-665.* 2021;12(1):654-665. doi:10.1364/BOE.405869
16. Zhu JY, Park T, Isola P, Efros AA. Unpaired Image-to-Image Translation using Cycle-Consistent Adversarial Networks. *Proceedings of the IEEE International Conference on Computer Vision.* 2017;2017-October:2242-2251. doi:10.1109/ICCV.2017.244
17. Tweel JED, Ecclestone BR, Boktor M, Simmons JAT, Fieguth P, Reza PH. Virtual Histology with Photon Absorption Remote Sensing using a Cycle-Consistent Generative Adversarial Network with Weakly Registered Pairs. Published online June 14, 2023. Accessed March 24, 2025. <https://arxiv.org/abs/2306.08583v2>
18. Chiaruttini N, Burri O, Haub P, Guet R, Sordet-Dessimoz J, Seitz A. An Open-Source Whole Slide Image Registration Workflow at Cellular Precision Using Fiji, QuPath and Elastix. *Front Comput Sci.* 2022;3:780026. doi:10.3389/FCOMP.2021.780026/BIBTEX
19. McHugh ML. Interrater reliability: the kappa statistic. *Biochem Med (Zagreb).* 2012;22(3):276-282.
20. Fleiss JL. Measuring nominal scale agreement among many raters. *Psychol Bull.* 1971;76(5):378-382. doi:10.1037/H0031619
21. Cohen J. A COEFFICIENT OF AGREEMENT FOR NOMINAL SCALES 1.
22. Altman DG. *Relation between Several Variables.*; 1999. Accessed March 4, 2025. <https://www.routledge.com/Practical-Statistics-for-Medical-Research/Altman/p/book/9781032836706>
23. R: a language and environment for statistical computing. Accessed March 4, 2025. <https://www.gbif.org/tool/81287/r-a-language-and-environment-for-statistical-computing>
24. Vicory J, Couture HD, Thomas NE, et al. Appearance normalization of histology slides. *Computerized Medical Imaging and Graphics.* 2015;43:89-98. doi:10.1016/J.COMPMEIMAG.2015.03.005
25. Bilgin CC, Rittscher J, Filkins R, Can A. Digitally adjusting chromogenic dye proportions in brightfield microscopy images. *J Microsc.* 2012;245(3):319-330. doi:10.1111/J.1365-2818.2011.03579.X

Photon Absorption Remote Sensing Virtual Histopathology

26. Li X, Plataniotis KN. A Complete Color Normalization Approach to Histopathology Images Using Color Cues Computed From Saturation-Weighted Statistics. *IEEE Trans Biomed Eng.* 2015;62(7):1862-1873. doi:10.1109/TBME.2015.2405791
27. Tosta TAA, de Faria PR, Neves LA, do Nascimento MZ. Color normalization of faded H&E-stained histological images using spectral matching. *Comput Biol Med.* 2019;111:103344. doi:10.1016/J.COMPBIOMED.2019.103344
28. Babic A, Loftin IR, Stanislaw S, et al. The impact of pre-analytical processing on staining quality for H&E, dual hapten, dual color in situ hybridization and fluorescent in situ hybridization assays. *Methods.* 2010;52(4):287-300. doi:10.1016/J.YMETH.2010.08.012
29. Bai B, Yang X, Li Y, Zhang Y, Pillar N, Ozcan A. Deep learning-enabled virtual histological staining of biological samples. *Light: Science & Applications* 2023 12:1. 2023;12(1):1-20. doi:10.1038/s41377-023-01104-7
30. Alam M, Armstrong A, Baum C, et al. Guidelines of care for the management of cutaneous squamous cell carcinoma. *J Am Acad Dermatol.* 2018;78(3):560-578. doi:10.1016/J.JAAD.2017.10.007
31. Bichakjian C, Armstrong A, Baum C, et al. Guidelines of care for the management of basal cell carcinoma. *J Am Acad Dermatol.* 2018;78(3):540-559. doi:10.1016/J.JAAD.2017.10.006
32. Nahhas AF, Scarbrough CA, Trotter S. A Review of the Global Guidelines on Surgical Margins for Nonmelanoma Skin Cancers. *J Clin Aesthet Dermatol.* 2017;10(4):37. Accessed March 3, 2025. <https://pmc.ncbi.nlm.nih.gov/articles/PMC5404779/>
33. Cives M, Mannavola F, Lospalluti L, et al. Non-Melanoma Skin Cancers: Biological and Clinical Features. *Int J Mol Sci.* 2020;21(15):5394. doi:10.3390/IJMS21155394
34. Atilla S, Gököz, Özer S, Elçin G. Concordance between a Mohs surgeon and a dermatopathologist in evaluating Mohs cryosections. *Journal of the European Academy of Dermatology and Venereology.* 2021;35(11):2219-2224. doi:10.1111/JDV.17574
35. Jagdeo J, Weinstock MA, Piepkorn M, Bingham SF. Reliability of the histopathologic diagnosis of keratinocyte carcinomas. *J Am Acad Dermatol.* 2007;57(2):279-284. doi:10.1016/J.JAAD.2007.03.021
36. Elder DE, Piepkorn MW, Barnhill RL, et al. Pathologist Characteristics Associated with Accuracy and Reproducibility of Melanocytic Skin Lesion Interpretation. *J Am Acad Dermatol.* 2018;79(1):52. doi:10.1016/J.JAAD.2018.02.070
37. Elmore JG, Barnhill RL, Elder DE, et al. Pathologists' diagnosis of invasive melanoma and melanocytic proliferations: observer accuracy and reproducibility study. *BMJ.* 2017;357:2813. doi:10.1136/BMJ.J2813
38. Du-Harpur X, Watt FM, Luscombe NM, Lynch MD. What is AI? Applications of artificial intelligence to dermatology. *British Journal of Dermatology.* 2020;183(3):423-430. doi:10.1111/BJD.18880

Photon Absorption Remote Sensing Virtual Histopathology

39. Takiddin A, Schneider J, Yang Y, Abd-Alrazaq A, Househ M. Artificial intelligence for skin cancer detection: Scoping review. *J Med Internet Res*. 2021;23(11). doi:10.2196/22934
40. Foltz EA, Witkowski A, Becker AL, et al. Artificial Intelligence Applied to Non-Invasive Imaging Modalities in Identification of Nonmelanoma Skin Cancer: A Systematic Review. *Cancers* 2024, Vol 16, Page 629. 2024;16(3):629. doi:10.3390/CANCERS16030629
41. Piepkorn MW, Longton GM, Reisch LM, et al. Assessment of Second-Opinion Strategies for Diagnoses of Cutaneous Melanocytic Lesions. *JAMA Netw Open*. 2019;2(10). doi:10.1001/JAMANETWORKOPEN.2019.12597
42. Gurina TS, Simms L. Histology, Staining. *StatPearls Publishing LLC*. Published online May 1, 2023. Accessed April 14, 2025. <https://www.ncbi.nlm.nih.gov/books/NBK557663/>
43. Wang SQ, Goldberg LH, Nemeth A. The merits of adding toluidine blue-stained slides in Mohs surgery in the treatment of a microcystic adnexal carcinoma. *J Am Acad Dermatol*. 2007;56(6):1067-1069. doi:10.1016/j.jaad.2007.01.008
44. Simmons JAT, Werezak SJ, Ecclestone BR, Tweel JED, Gaouda H, Reza PH. Label-Free Non-Contact Structural and Functional Vascular Imaging using Photon Absorption Remote Sensing. Published online October 8, 2023. Accessed March 3, 2024. <https://arxiv.org/abs/2310.05260v1>